Chemical Tuning of Structure, Magnetization, and Conductivity in the Self-doped Double-Perovskite $(Sr_{2-x}Ca_x)FeMoO_6$ ($0 \leq x \leq 2.0$) System

T. S. Chan,[†] R. S. Liu,*[,†] G. Y. Guo,[‡] S. F. Hu,[§] J. G. Lin,[||] J. M. Chen,[⊥] and J. P. Attfield[#]

Departments of Chemistry and Physics, and Center for Condensed Matter Sciences, National Taiwan University, Taipei, Taiwan, Republic of China, National Nano Device Laboratories, Hsinchu, Taiwan, Republic of China, Synchrotron Radiation Research Center, Hsinchu, Taiwan, Republic of China, and Department of Chemistry, University of Cambridge, Lensfield Road, Cambridge CB2 1EW, United Kingdom

Received July 22, 2002. Revised Manuscript Received October 24, 2002

The variations of crystal structure, magnetization, and conductivity resulting from the chemical pressure effects of substituting Sr^{2+} by the smaller Ca^{2+} in the double-perovskite $(Sr_{2-x}Ca_x)FeMoO_6$ have been investigated. An increase in the Ca content leads to an increase in the Fe/Mo ordering in the materials, which raises the magnetic moments close to the theoretical value of 4 μ_B. An increase in conductivity with increasing Ca content is also found and is consistent with an increase in $(Fe^{2+} + Mo^{6+})/(Fe^{3+} + Mo^{5+})$ band overlap rather than bandwidth changes. The changes observed by physical measurements are supported by the X-ray absorption near-edge structures of Fe and Mo and by band structure calculations.

Introduction

Half-metallic compounds which have electrons with only one spin direction at the Fermi level have recently received considerable attention for their potential applications in spintronics.[1] Several magnetic oxides have been identified as having half-metallic behavior at low temperatures; however, their spin polarization is strongly reduced at room temperature (RT).[2] Therefore, oxides with both high spin polarization and high Curie temperatures are of particular interest. Recently, Kobayashi et al.[3] reported a high spin polarization for an oxide material with a double-perovskite structure, Sr_2FeMoO_6 which also has a high Curie temperature, ($T_c = 420$ K).

In Sr_2FeMoO_6, the Fe^{2+} or Fe^{3+} ions are in a high-spin state with all the spin-up 3d orbitals occupied. Sleight and Weiher[4] proposed that if the spin-down 3d orbitals of Fe have similar energy to the 4d orbitals of Mo, the empty spin-down states ($\pi^*-\beta$) of Fe^{3+} are degenerate to the one-electron occupied spin-down states ($\pi^*-\beta$) of Mo^{5+} which may lead to the formation of a narrow band. The electrons in this band have antiparallel spins to the localized spins in the spin-up states ($\sigma^*-\alpha$ and $\pi^*-\alpha$) of Fe^{3+}. A ferromagnetic half-metallic state is thus observed in this ordered perovskite with localized up-spins of Fe^{3+} and itinerant spin-down electron of Mo^{5+}. This is supported by the band calculations, which show at the Fermi level a mixing of the spin-down O 2p, Fe 3d, and Mo 4d bands.[3,5,6] This band description is equivalent to an internal redox equilibrium between $(Fe^{2+} + Mo^{6+})$ and $(Fe^{3+} + Mo^{5+})$ states.

Further studies on other members of the $A_2BB'O_6$ (where A = alkaline-earth or rare-earth ion and B and B′ = transition metal ion) family of double perovskites show that the occurrence of magnetoresistance (MR) properties is a fairly common feature. The A = Ca and Ba analogues of A_2FeMoO_6 were also found to display half-metallic and ferrimagnetic properties.[7−10] Moreover, the A_2FeReO_6 (A = Ca, Sr, Ba) compounds exhibit[11,12] a half-metallic ground-state concomitant with ferrimagnetic coupling of Fe^{3+} and Re^{5+} ($5d^2$, $S = 1$) magnetic moments and show MR at RT. It is thus of great interest to explore other prospective half-metallic compounds with large MR effects at low magnetic fields,

* To whom correspondence should be addressed. E-mail: rsliu@ccms.ntu.edu.tw.
[†] Department of Chemistry, National Taiwan University.
[‡] Department of Physics, National Taiwan University.
[||] Center for Condensed Matter Sciences, National Taiwan University.
[§] National Nano Device Laboratories.
[⊥] Synchrotron Radiation Research Center.
[#] University of Cambridge.

(1) Prinz, G. *Science* **1998**, *282*, 1660.
(2) Gupta, A.; Sun, J. Z. *J. Magn. Magn. Mater.* **1999**, *200*, 24.
(3) Kobayashi, K.-I.; Kimura, T.; Sawada, H,; Terakura, K.; Tokura, Y. *Nature* **1998**, *395*, 677.
(4) Sleight, A. W.; Weiher, J. F. *J. Phys. Chem. Solids* **1972**, *33*, 679.
(5) Kim, T. H.; Uehara, M.; Cheong, S. W.; Lee, S. *Appl. Phys. Lett.* **1999**, *74*, 1737.
(6) Fang, Z.; Terakura, K.; Kanamoru, J. *Phys. Rev. B* **2001**, *63*, 180407.
(7) Maignan, A.; Raveau, B.; Martin, C.; Hervieu, M. *J. Solid State Chem.* **1999**, *59*, 11159.
(8) Alonso, J. A.; Casais, M. T.; Martínze-Lope, M. J.; Velasco, P.; Muñoz, A.; Fernández-Díaz, M. T. *Chem. Mater.* **2000**, *12*, 161.
(9) Borges, R. P.; Thomas, R. M.; Cullinan, C.; Coey, J. M. D.; Suryanarayan, R.; Ben-Dor, L.; Pinsard-Gaudart, L.; Revcolevschi, A. *J. Phys. Condens. Matter* **1999**, *11*, L445.
(10) Ritter, C.; Ibarra, M. R.; Morellón, L.; Blasco, J.; García, J.; De Teresa, J. M. *J. Phys.: Condens. Matter* **2000**, *12*, 8295.
(11) Prellier, W.; Smolyaninova, W.; Bisbas, A.; Galley, C.; Greene, R. L.; Ramesha, K.; Gopalakrishnan. J. *J. Phys. Condens. Matter* **2000**, *12*, 965.
(12) Kobayashi, K.-I.; Kimura, T.; Sawada, H.; Terakura, K.; Tokura, Y. *Phys. Rev. B* **1999**, *59*, 11159.

10.1021/cm020773h CCC: $25.00
Published on Web 12/17/2002

in ferromagnetic compounds with T_c as close to RT as possible. Studies of polycrystalline samples,[3,5,6,9,13] epitaxial thin films[14,15] and artificial grain boundaries[16] have demonstrated that the negatively spin-polarized conduction is the origin of the extrinsic, strong MR associated with spin-polarized tunneling between adjacent grains. This is known as tunneling magnetoresistance (TMR). A better understanding of the factors that control the structural, magnetic, and conduction properties of these compounds is critical for optimizing their properties for the applications based on their TMR effects.

In a recent report, Goodenough and Dass[17] first report on the series samples of $Sr_{2-x}Ca_xFeMoO_6$, $0 \le x \le 2$. They found that ferromagnetic long-range ordered domains are coupled antiferromagnetically across antiphase boundaries; random disorder within domains may be small. In this article we aim to investigate in detail the variation of crystal structure and magnetic properties of the $(Sr_{2-x}Ca_x)FeMoO_6$ ($0 \le x \le 2.0$) double-perovskite system due to chemical substitution of the smaller Ca^{2+} ions for the bigger Sr^{2+} cations, which applies an internal chemical pressure. We report systematic structural phase changes from tetragonal to monoclinic symmetry and a decrease in the refined Fe/Mo anti-site disorder at $x \ge 1.5$. Most interestingly, we demonstrate the dramatic changes in the magnetic and transport properties upon tuning the Ca doping amount in the Sr site, which enhances the TMR properties described previously for Sr_2FeMoO_6.

Experimental Section

Sample Preparation. The samples of $(Sr_{2-x}Ca_x)FeMoO_6$ ($0 \le x \le 2.0$) were prepared by the solid-state reaction method. Stoichiometric mixtures of high-purity oxides $SrCO_3$, $CaCO_3$, Fe_2O_3, and MoO_3 were first calcined in air at 800 °C for 12 h. The obtained powders were ground and pressed into pellets (15 mm in diameter and 3 mm in thickness). The pellets of $(Sr_{2-x}Ca_x)FeMoO_6$ ($0 \le x \le 1.5$) were sintered at 1000 °C for 38 h in a 5% H_2/N_2 gas mixture, and the pellet with $x = 2.0$ was sintered at 1200 °C for 12 h in a 5% H_2/N_2 gas mixture.

Characterization. X-ray diffraction (XRD) measurements were carried out on a SCINTAG (X1) diffractmeter (Cu Kα radiation, $\lambda = 1.5406$ Å) at 40 kV and 30 mA. The GSAS program[18] was used for the Rietveld refinements to obtain information on the crystal structures of $(Sr_{2-x}Ca_x)FeMoO_6$. A pseudo-Voigt function was chosen to generate the line shape of the diffraction peaks. In the final runs, the positional coordinates, isotropic thermal factors, and anti-site disorder of Mo and Fe atoms were refined. Scanning electron micrographs (SEMs) were measured at room temperature by a Philips XL30 SEM equipped with a field emission gun at 15 kV. Electron diffraction (ED) and high-resolution transmission electron microscopy (HRTEM) were carried out using a JEOL 4000EX electron microscope operated at 400 kV. Image simulation was made using CaRIne software. The samples for microscopic measurement were dispersed in alcohol before being transferred to the carbon-coated copper grids. The resistively measurements at zero field [($\rho(T)$)] and under a magnetic field [($\rho(H)$)] were performed with a Quantum Design PPMS (physical properties measurements system), using the conventional four-probe technique, under magnetic fields up to 3 T. Magnetization measurements were performed on a SQUID magnetometer from 0 to 350 K.

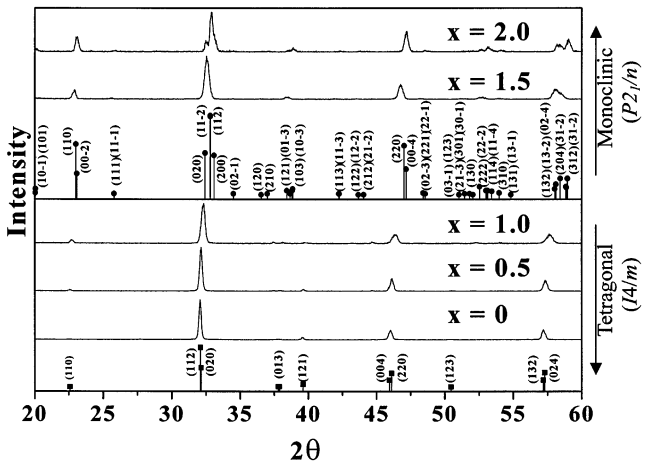

Figure 1. XRD patterns for $(Sr_{2-x}Ca_x)FeMoO_6$, indexed on a tetragonal unit cell ($I4/m$) for $x = 0$, 0.5, and 1, and indexed in a monoclinic unit cell ($P2_1/n$) for $x = 1.5$ and 2.0.

X-ray Absorption Measurements. X-ray absorption near-edge structure (XANES) measurements at Fe L_{23} and Mo M_{23} edges were performed at the synchrotron radiation research center (SRRC) in Hsinchu, Taiwan, with an electron beam energy of 1.5 GeV and a maximum stored current of 240 mA. The spectra were recorded by measuring the sample current. The incident photon flux (I_0) was monitored simultaneously by using a Ni mesh located after the exit slit of the monochromatic beam. All the measurements were performed at room temperature. The reproducibility of the adsorption spectra of the same sample in different experimental runs was found to be extremely good.

Band Structure Calculated. Band structures of tetragonal ($x = 0$) and monoclinic ($x = 2.0$) $(Sr_{2-x}Ca_x)FeMoO_6$ were calculated using the all-electron full-potential theory linear augmented plane wave (FLAPW) method.[19] These calculations are based on first-principles density functional theory (DFT) with the generalized gradient approximation (GGA) to the exchange-correlation potential.[20] Fe 4s4p3d, Mo 5s5p4d, O 2s2p, Sr 5s5p5d, and Ca 4s4p3d are treated as band states. The shallow Fe:3s3p, Mo:4s4p, Sr:4s4p, and Ca:3s3p orbitals were also treated as band states by using the so-called local orbitals. A large number (≈120/atom) of augmented plane waves were used. The wave function, charge densities, and potentials were expanded in terms of the spherical harmonics inside the muffin-tin spheres with $L_{max} = 10$, 6, and 6, respectively. The number of k-points in the irreducible Brillouin zone wedge used in the tetrahedron integration method[21] is 288 for the tetrahedral structure and 130 for the monoclinic structure.

Results and Discussion

The powder XRD patterns of the $(Sr_{2-x}Ca_x)FeMoO_6$ ($0 \le x \le 2.0$) samples are shown in Figure 1. Each composition of the series is single phase. For the samples with $x < 1.0$ and $x > 1.5$, all the peaks in each

(13) García-Landa, B.; Ritter, C.; Ibarra, M. R.; Blasco, J.; Algarabel, P. A.; Mahendiran, R.; García, *J. Solid State Commun.* **1999**, *110*, 435.
(14) Lu, K. Q.; Stern, E. A. *Nucl. Instrum. Methods* **1983**, *212*, 475.
(15) Manako, T.; Izumi, M.; Konishi, Y.; Kobayashi, K.-I.; Kawasaki, M.; Tokura, Y. *Appl. Phys. Lett.* **1999**, *74*, 2215.
(16) Yin, H. Q.; Zhou, J. S,; Zhou, J. P.; Dass, R.; McDevitt, J. T.; Goodenough, J. B. *Appl. Phys. Lett.* **1999**, *75*, 2812.
(17) Goodenough, J. B.; Dass, R. I. *Int. J. Inorg. Mater.* **2000**, *2*, 3.
(18) Larson, A. C.; Von Dreele, R. B. *Generalized Structure Analysis System* (*GSAS*); Los Alamos National Laboratory Report LAUR 86-748; Los Alamos National Laboratory: Los Alamos, NM, 1994.
(19) Blaha, P.; Schwarz, K.; Madsen, G. K. H.; Kvasnicka, D.; Luitz, J., *WIEN2k, An Augmented Plane Wave + Local Orbitals Program for Calculating Crystal Properties*; Karlheinz Schwarz, Techn. Universitat Wien: Austria, 2001; ISBN 3-9501031-2.
(20) Perdew, J. P.; Burke, S.; Ernzerhof, M. *Phys. Rev. Lett.* **1996**, *77*, 3865.
(21) Bloechl, P. E.; Jepsen, O.; Andersen, O. K. *Phys. Rev. B* **1991**, *44*, 943.

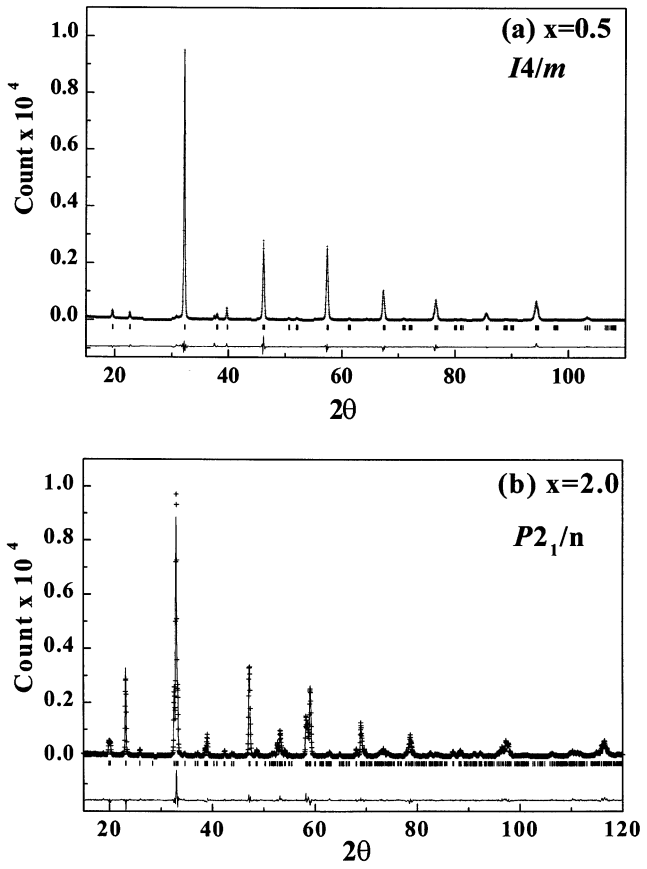

Figure 2. Rietveld fits to powder XRD data for $(Sr_{2-x}Ca_x)FeMoO_6$ with (a) $x = 0.5$, space group $I4/m$, and (b) $x = 2.0$, space group $P2_1/n$, at 300 K. Observed (plus signs) and calculated (solid line) intensities are shown with the difference at the bottom.

pattern can be indexed on the basis of a tetragonal unit cell (space group: $I4/m$) and monoclinic (space group: $P2_1/n$), respectively. This indicates that in the $x = 1-1.5$ region the structure changes from tetragonal to monoclinic at RT. The initial structural models fitted with the Rietveld profile method were based on Sr_2FeMoO_6 for $x = 0$, 0.5, and 1.0[22] and Ca_2FeMoO_6 for $x = 1.5$ and 2.0.[8] Figure 2a,b displays the observed and calculated X-ray powder diffraction profiles at 300 K of $(Sr_{2-x}Ca_x)FeMoO_6$ with $x = 0.5$ and 2.0. All the observed peaks can be fitted with the reflection conditions of the space groups $I4/m$ for $x = 0.5$ and $P2_1/n$ for $x = 2.0$, respectively. Free refinement of the atomic positions was possible for all samples except those on either side of the structural transition ($x = 1.0$ and 1.5). For these materials, the coordinates were fixed, at the $x = 0.5$ values for the $x = 1.0$ refinement, and at the $x = 2.0$ values for the $x = 1.5$ refinement. In the final refinements, the possibility of anti-site disordering due to some Mo sites being occupied by Fe atoms and vice versa was taken into account. The atomic parameters derived from typical refinements are given in Table 1. The final lattice parameters of the series $(Sr_{2-x}Ca_x)FeMoO_6$ ($0 \le x \le 2.0$) samples are given in Table 2 and derived distances and angles are shown in Table 3. The refined occupancies of the Fe and Mo sites in Table 2 show that the Fe/Mo anti-site disorder is abruptly decreased in

Table 1. Atomic Positions, Isotropic Temperature Factors, and Occupancies for $(Sr_{2-x}Ca_x)FeMoO_6$ with (a) $x = 0.5$ and (b) $x = 2.0$

atoms	*x*	*y*	*z*	U_{iso} (Å^2)	occupancy
			(a) $x = 0.5$		
Sr	0.5	0	0.25	0.0312(6)	0.771(7)
Ca	0.5	0	0.25	0.0312(6)	0.229(7)
Fe1	0	0	0	0.0262(6)	0.889(4)
Mo2	0	0	0.5	0.0262(6)	0.889(4)
Mo1	0	0	0	0.0262(6)	0.111(4)
Fe2	0	0	0.5	0.0262(6)	0.111(4)
O1	0	0	0.2527(3)	0.0533(1)	1
O2	0.25	0.25	0	0.0533(1)	1
			(b) $x = 2.0$		
Ca	0.9898(8)	0.0456(3)	0.2485(4)	0.0168(4)	1
Fe1	0.5	0	0.5	0.0132(2)	0.923(4)
Mo2	0.5	0	0	0.0132(2)	0.923(4)
Mo1	0.5	0	0.5	0.0132(2)	0.077(4)
Fe2	0.5	0	0	0.0132(2)	0.077(4)
O1	0.0858(1)	0.4783(1)	0.2530(1)	0.0130(1)	1
O2	0.7000(1)	0.2921(1)	0.0572(1)	0.0130(1)	1
O3	0.2077(1)	0.2069(1)	0.9594(2)	0.0130(1)	1

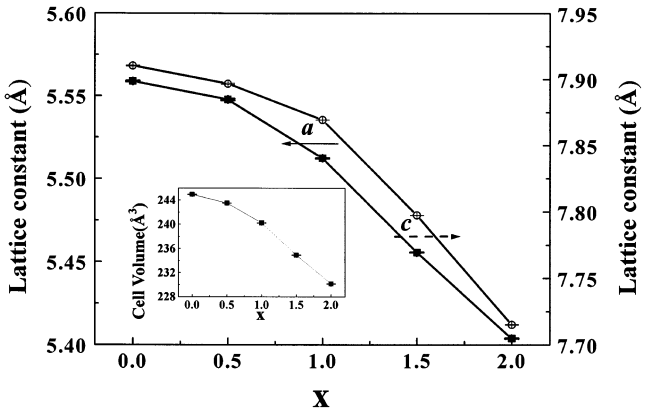

Figure 3. Lattice constants (a and c) as a function of x in $(Sr_{2-x}Ca_x)FeMoO_6$ ($0 \le x \le 2.0$). The cell volume as a function of x is shown in the inset.

$x = 2.0$ of $(Sr_{2-x}Ca_x)FeMoO_6$. Recently, Alonso and coworkers[23] proposed that the actual degree of order depends mainly on the synthesis conditions. Therefore, an increase in order of the $x = 2.0$ sample may be due to the higher synthesis temperature (1200 °C). The lattice parameters (a and c) and cell volume (inset of Figure 3) decrease with increasing Ca content as noted from Table 2 and Figure 3, due to the substitution of the smaller Ca^{2+} ions (1.34 Å) for the larger Sr^{2+} (1.44 Å) cations.[24] Importantly, these structural parameters indicate that the structure phase transition is continuous.

The morphology and particle size of the $(Sr_{2-x}Ca_x)FeMoO_6$ ($0 \le x \le 2.0$) samples probed by SEM are shown in Figure 4. An increase of particle size with increasing Ca content (from ~1 μm at $x = 0$ to ~2 μm at $x = 2.0$) was observed. This indicates that the incorporation of Ca into Sr sites facilitates grain growth during the sintering process.

Parts a and b of Figure 5 show a typical ED pattern and HRTEM lattice image, respectively, recorded along the [001] zone-axis direction of Sr_2FeMoO_6. The simulated pattern along zone axis [001] is shown in Figure

(22) Chmaissem, O.; Kruk, R.; Dabrowski, B.; Brown, D. E.; Xiong, Z.; Kolesnik, S.; Jorgensen, J. D. *Phys. Rev. B* **2000**, *62*, 14197.

(23) Sánchez, D.; Alonso, J. A.; García-Hernández, M.; Martínze-Lope, M. J.; Martínez, J. L. *Phys. Rev. B* **2002**, *65*, 104426.

(24) Shannon, R. D. *Acta Crystallogr., A* **1976**, *32*, 751.

Table 2. Structure Parameters, Fe/Mo Anti-site Occupancy, and Saturation Magnetization (μ_B) for $(Sr_{2-x}Ca_x)FeMoO_6$ ($0 \le x \le 2.0$)[a]

compounds	a (Å)	b (Å)	c (Å)	β	V (Å^3)	R_p (%)	R_{wp} (%)	χ^2	Fe/Mo anti-site	μ_B
$x = 0$	5.5686(3)	5.5686(3)	7.8985(4)	90°	244.93(2)	7.73	11.82	1.44	15.1%	2.56
$x = 0.5$	5.5573(4)	5.5573(4)	7.8847(6)	90°	243.51(3)	8.66	13.52	1.78	11.1%	3.23
$x = 1.0$	5.5355(1)	5.5355(1)	7.8403(3)	90°	240.24(1)	10.58	16.58	4.54	13.4%	3.03
$x = 1.5$	5.4780(1)	5.5195(9)	7.7695(1)	90.39°(9)	234.91(7)	11.97	15.93	4.23	11.4%	3.82
$x = 2.0$	5.4121(2)	5.5183(2)	7.7046(3)	90.04°(6)	230.13(1)	7.96	10.88	1.96	7.7%	3.99

[a] Reliability factors after the Rietveld refinement are also given.

Table 3. Main Bond Distances (Å) and Selected Angles (deg) for $(Sr_{2-x}Ca_x)FeMoO_6$ ($0 \le x \le 2.0$) Determined from XRD Data at 300 K

sample	$x = 0$	$x = 0.5$	$x = 1.0$	sample	$x = 1.5$	$x = 2.0$
dFe1−O1 ×2	1.968(1)	1.946(1)	1.917(2)	dFe1−O1 ×2	2.039(3)	2.019(1)
dFe1−O2 ×4	1.969(1)	1.965(1)	1.957(3)	dFe1−O2 ×2	2.044(3)	2.037(7)
dMo2−O1 ×2	1.982(2)	1.996(1)	2.005(2)	dFe1−O3 ×2	1.997(2)	1.990(7)
dMo2−O2 ×4	1.969(1)	1.965(1)	1.957(3)	dMo2−O1 ×2	1.965(3)	1.951(1)
				dMo2−O2 ×2	2.005(3)	1.996(7)
				dMo2−O3 ×2	1.998(2)	1.981(7)
⟨Fe1−O⟩	1.969(1)	1.959(1)	1.944(2)	⟨Fe1−O⟩	2.027(3)	2.015(6)
⟨Mo2−O⟩	1.973(1)	1.975(1)	1.973(2)	⟨Mo2−O⟩	1.989(3)	1.976(6)
∠Fe1−O1−Mo2	180	180	180	∠Fe1−O1−Mo2	152.00(7)	152.09 (3)
∠Fe1−O2−Mo2	180	180	180	∠Fe1−O2−Mo2	147.54(4)	147.50(5)
				∠Fe1−O3−Mo2	153.43(3)	153.50(6)

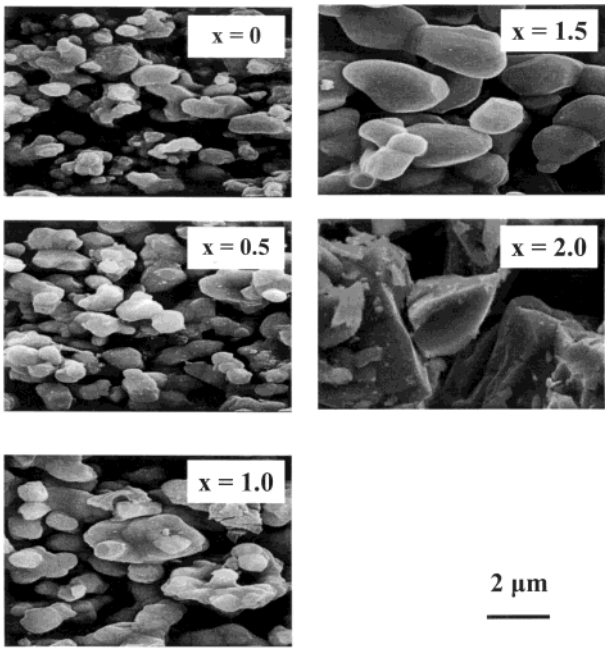

Figure 4. SEM photographs of $(Sr_{2-x}Ca_x)FeMoO_6$ ($0 \le x \le 2.0$)

5c. The cell symmetry obtained by ED was identified by observation only of hkl; $h + k + l = 2n$ reflections, indicating I-centering of the unit cell which is consistent with the XRD refinement result. Moreover, the HRTEM lattice image shows a tetragonal cell with $a = b \sim 5.57$ Å. In parts a and b of Figure 6 are the typical ED pattern and the HRTEM lattice image recorded along the [111] zone-axis direction of Ca_2FeMoO_6. The simulated pattern along the [111] zone axis is shown in Figure 6c. The agreement between experimental and calculated [111] HRTEM images confirms the correctness of the structural model.

Figure 7 shows the temperature dependence of high-field ($H = 5$ T) magnetizations of $(Sr_{2-x}Ca_x)FeMoO_6$ ($0 \le x \le 2.0$) samples. The substitution of Sr^{2+} by Ca^{2+} systematically increases the ferromagnetism, although the magnetizations of the $x = 1.0$ sample is anomalously low and is below that of the $x = 0.5$ sample. The magnetization isotherms of $(Sr_{2-x}Ca_x)FeMoO_6$ are typically ferromagnetic with negligible remanence and coercivity as illustrated in Figure 8. The saturation magnetizations at 5 K for all the studied compounds are listed in Table 2. For the $x \ge 1.5$ samples, the obtained values are consistent with a ferromagnetic state near the expected 4 μ_B fu^{-1} for a nominal ionic configuration Fe^{3+} ($S = {}^5/_2$)/Mo^{5+} ($S = {}^1/_2$). However, in $x < 1.5$ samples, the observed total magnetic moment is smaller than the expected value. This variation can be attributed to the effect of anti-site disorder at the octahedral Fe, Mo cation sublattices.[10,25] The anti-site cation occupancy, p, ideally reduces the net moment to $4 - 2p$ μ_B fu^{-1}; however, the local magnetic disorder caused by the anti-site defects reduces the ordered moment still further.

The transport properties of $(Sr_{2-x}Ca_x)FeMoO_6$ ($x = 0.5$, 1.0, and 2.0) are illustrated in Figure 9 a. Both $\rho(H = 0)$ and $\rho(H = 3$ T) show a semi-metallic behavior over the whole temperature range, down to 5 K. The observed value for $x = 2.0$, ρ ($T = 300$ K, $H = 0$), of $2 \times 10^{-3}\Omega$ cm is considerably smaller than that of the Sr doped analogues ($x = 0.5$ and 1.0). Alonso et al.[8] proposed that the high values indicate that the carrier scattering at the grain boundaries dominates the resistivity of the Sr- and Ba-containing samples. The Ca-doped samples, which are characterized by a homogeneous particle size, probably have an improved connectivity so that the measurements provide a better approximation of the bulk (integrated) resistivity. The more metallic behavior observed for the Ca-doped materials suggests a higher degree of electronic itinerancy.

The magnetotransport properties are shown as the evolution of MR (3 T), defined as $MR(T, H) = [\rho(T, H{=}0) - \rho(T, H{=}3\text{ T})]/\rho(T, H{=}3\text{ T})$, in Figure 9b. The highest MR ratio appears in the $x = 2.0$ sample, which has a low Fe/Mo anti-site disorder and the highest magnetiza-

(25) Ogale, A. S.; Ogale, S. B.; Ramesh, R.; Venkatesan, T. *Appl. Phys. Lett.* **1999**, *75*, 537.

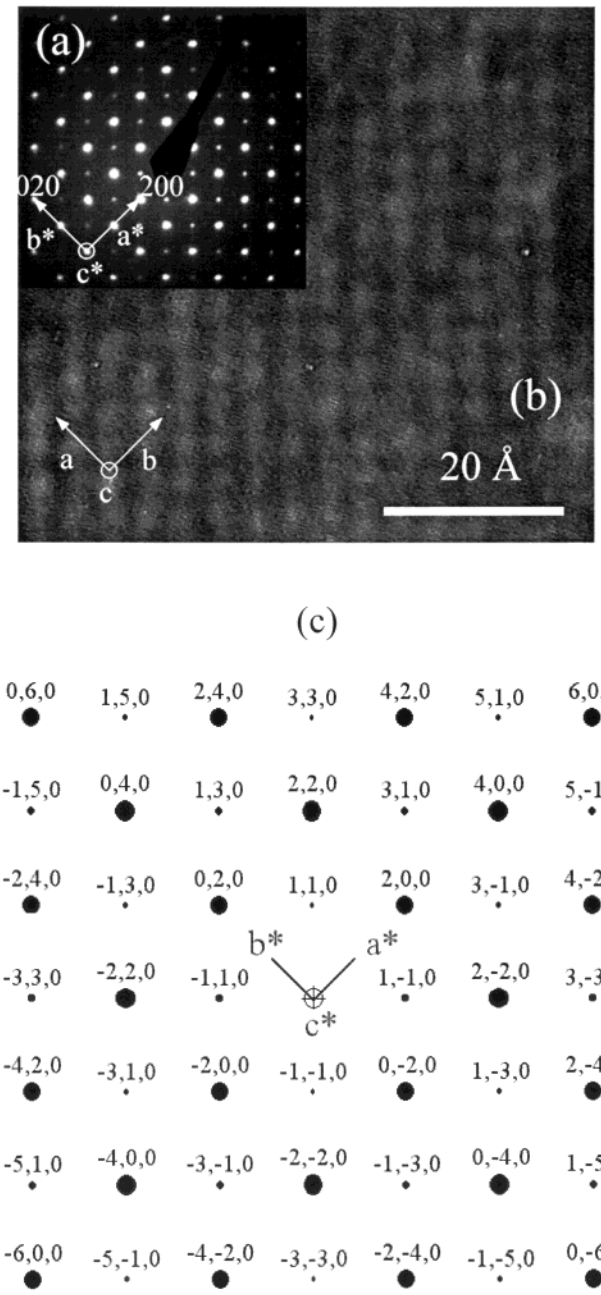

Figure 5. (a) ED pattern and (b) HRTEM lattice image along the [001] direction of the $(Sr_{2-x}Ca_x)FeMoO_6$ ($x = 0$) sample. (c) Simulated pattern along the zone axis [001].

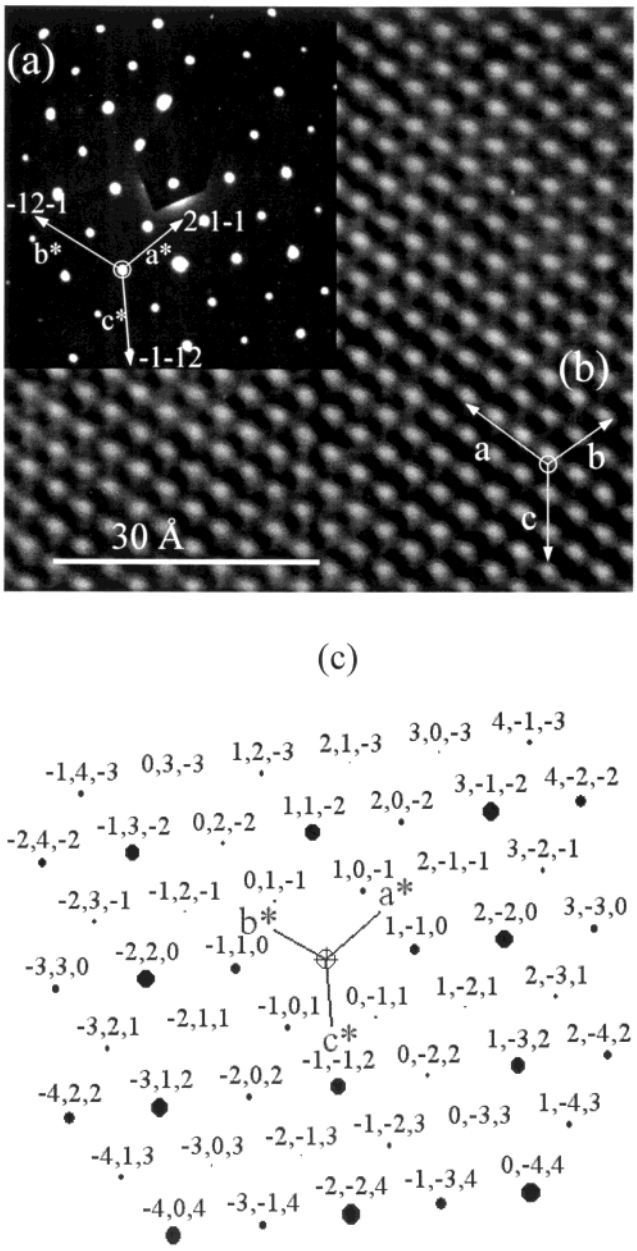

Figure 6. (a) ED pattern and (b) HRTEM lattice image along the [111] direction of $(Sr_{2-x}Ca_x)FeMoO_6$ ($x = 2$) sample. (c) Simulated pattern along the zone axis [111].

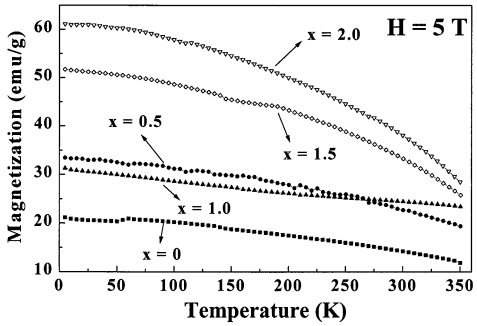

Figure 7. Temperature dependence of high-field ($H = 5$ T) magnetization of the $(Sr_{2-x}Ca_x)FeMoO_6$ ($0 \le x \le 2.0$).

tion. However, the $x = 2.0$ sample has a much lower T_c ($T_c \sim 377$ K),[8] which makes it less interesting than that of the $x = 0$ sample ($T_c = 420$ K).[3] Lower MR ratios are found in the $x \le 1.0$ samples, which have a higher Fe/Mo disorder and lower magnetizations. The anti-site chemical substitution is known to lower the MR ratio in Sr_2FeMoO_6 samples.[26,27]

The Fe L-edge XANES spectra of $(Sr_{2-x}Ca_x)FeMoO_6$ ($x = 0$, 0.5, 1.0, and 1.5) are shown in Figure 10a. For comparison, the spectra of FeO, Fe_3O_4, and Fe_2O_3 are also plotted. The spectra show two broad multiplet structures separated by spin−orbit splitting (of Fe $2p_{3/2}$ and $2p_{1/2}$). The chemical shift does not vary significantly, although the Fe profile changes systematically when the Ca content is increased from $x = 0$ to $x = 1.5$. It is well-

(26) Sarma, D. D.; Sampathkumaran, E. V.; Ray, S.; Nagarajan, R.; Majumdar, S.; Kumar, A.; Nalini, G.; Guru Row, T. N. *Solid State Commun.* **2000**, *114*, 465.

(27) Arulraj, A.; Ramesha, K.; Gopalakrishnan, J.; Rao, C. N. *J. Solid State Chem.* **2000**, *155* 233.

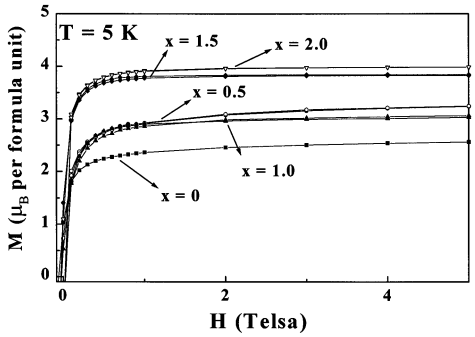

Figure 8. Magnetization isotherms of $(Sr_{2-x}Ca_x)FeMoO_6$ ($0 \leq x \leq 2.0$) at 5 K.

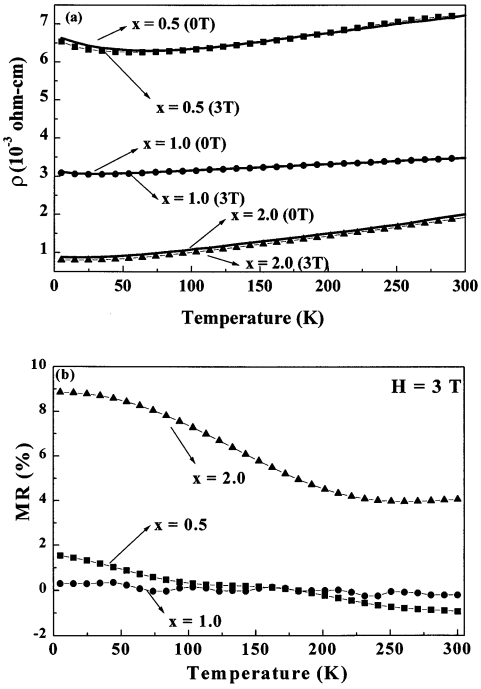

Figure 9. (a) Temperature dependence of resistivity of the $(Sr_{2-x}Ca_x)FeMoO_6$ ($x = 0.5$ and 1.0) samples. Effect of a magnetic field of 3 T is shown. (b) Plot of MR against temperature for $(Sr_{2-x}Ca_x)FeMoO_6$ ($x = 0.5$, 1.0, and 2.0).

established that an effective Fe valence can be measured from the peak width at the Fe 2p X-ray adsorption edge in FeO and Fe_2O_3.[28] We therefore adopted the same scheme to obtain the Fe valence. As deduced from Figure 10a, the Fe valence is much greater than 2+ but less than 3+ over the range of Ca substitution. Here, the relative intensity ratio of the energy at 710 and 708 eV [as denoted by $I(710)/I(708)$] corresponding to the ratio of $Fe^{3+}$and Fe^{2+} increases with x as shown in the inset of Figure 10a. The average valence for Fe has also been found to be intermediate between high-spin configuration values of Fe^{2+} and Fe^{3+} from Mössbauer spectroscopy studies.[8,29] From the chemical formula $(Sr_{2-x}Ca_x)FeMoO_6$, assuming oxygen stoichiometry, if the valence of Fe is $2 + y$, then Mo should formally be in the $6 - y$ state. In Figure 10b, the Mo M-edge absorption spectra of $(Sr_{2-x}Ca_x)FeMoO_6$ along with those of MoO_2 (Mo^{4+}), and MoO_3 (Mo^{6+}) standards are shown. The intense peaks at the Mo M-edge onset involve 3p-

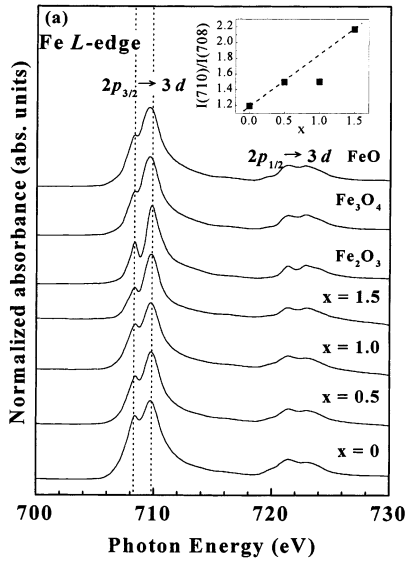

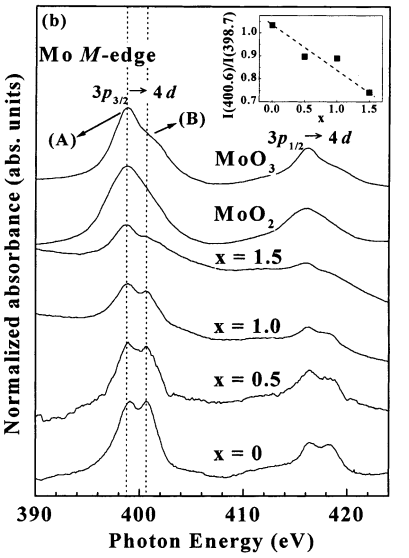

Figure 10. (a) Fe 2p-edge X-ray absorption near-edge structure spectra of FeO (Fe^{2+}), Fe_3O_4 ($Fe^{2.67+}$), Fe_2O_3 (Fe^{3+}), and $(Sr_{2-x}Ca_x)FeMoO_6$ ($x = 0$, 0.5, 1.0, and 1.5). (b) Mo 3p-edge X-ray absorption near-edge structure spectra of MoO_2 (Mo^{4+}), MoO_3 (Mo^{6+}), and $(Sr_{2-x}Ca_x)FeMoO_6$ ($x = 0$, 0.5, 1.0, and 1.5).

core to 4d final-state transitions. These features can provide a probe of the 4d states, albeit modified by a transition matrix element, core−hole-interaction, and multiplet effects.[30] Two strong spectral features are clearly visible in the MoO_3 standard: the low-energy peak (A), due to the 3p to 4d t_{2g} excitations, and the high-energy peak (B), due to 3p to $4d_{eg}$ excitations. A clear decrease in the relative (B)-feature strength strongly supports the Mo-valence reduction with the increasing Ca content, which is shown in the inset of Figure 10b. The relative intensity ratio of the energy of 400.6 and 398.7 eV [as denoted by $I(400.6)/I(398.7)$] corresponding to the ratio of Mo^{6+} and Mo^{4+} decreases with an increase in x. Moreover, the Mo valence is consistent with a significant value of $y < 1$ in the formal value of $6 - y$.

To discuss the anticipated half-metallic features, we first show the electronic structures of double-perovskites

(28) Martine, G. S. *J. Eur. Ceram. Soc.* **1998**, *18*, 2253.
(29) Woodward, P. M. *Acta Crystallogr., Sect. B* **1997**, *53*, 32.
(30) Zeng, Z.; Fawcett, I. D.; Greenblatt, M.; Croft, M. *Mater. Res. Bull.* **2001**, *36*, 705.

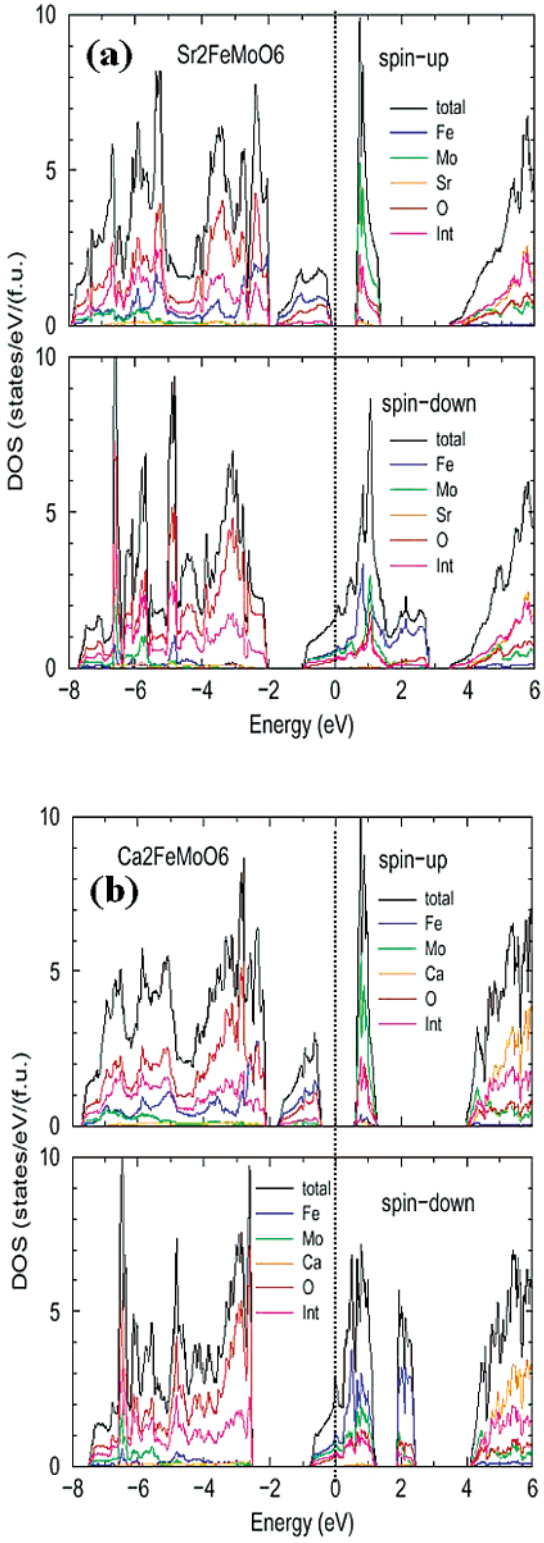

Figure 11. Total and site-decomposed density of states (D.O.S.) of $(Sr_{2-x}Ca_x)FeMoO_6$ (a) $x = 0$ and (b) $x = 2.0$.

$(Sr_{2-x}Ca_x)FeMoO_6$ ($x = 0$ and $x = 2.0$), calculated by the full-potential augmented plane-wave (FLAPW) method. The calculations were based on the Rietveld refined models of $x = 0$ with the tetragonal unit cell and $x = 2.0$ with the monoclinic unit cell. The density of states obtained by this calculation is shown in Figure 11 a for $x = 0$ and 11b for $x = 2.0$. At the Fermi level (E_F), the density of states is non-zero only in the spin-down band. The occupied spin-up band just below E_F mainly consists of Fe 3d electrons forming the localized spins on the Fe sites. In contrast, the spin-down band around E_F is made up of hybridized Fe 3d t_{2g} and Mo 4d t_{2g} states. The predicted electronic features for Sr_2FeMoO_6 resembles those calculated by Kobayashi et al.[3] and Fang et al.[6] Compared to Sr_2FeMoO_6, the change in the spin-up band of Ca_2FeMoO_6 is minor, but the change in the spin-down band is significant. A splitting of the hybridized Fe 3d t_{2g} and Mo 4d t_{2g} bands is observed in Ca_2FeMoO_6 for the first time, which may be due to the decrease in structural symmetry compared to that of Sr_2FeMoO_6. Moreover, the density of states of the $(Sr_{2-x}Ca_x)FeMoO_6$ ($x = 2.0$) sample in the spin-down band has a local peak at E_F and so is strongly enhanced (by 1.5 times) compared to the $x = 0$ sample, which is consistent with the resistivity results (the $x = 2.0$ sample has a higher conductivity than the $x = 0$ sample).

For perovskite ABX_3 compounds, the bandwidth W depends on both the B−X−B bond angles and B−X bond lengths, through the overlap integrals between the 3d orbitals of the metal ion B and the 2p orbitals of the X anion in the tight-binding approximation. The following formula has been applied to describe this double dependence:[31]

$$W \propto \frac{\cos \omega}{d_{B-X}^{3.5}}$$

where ω (given by $^1/_2[\pi-(B-X-B)]$) is the "tilting" angle in the plane of the bond and d_{B-X} is the B−X bond length. The dominant structural change across the series $(Sr_{2-x}Ca_x)FeMoO_6$ is the decrease in B−X−B bond angles as shown in Table 3. This indicates that the application of chemical pressure by substituting smaller Ca^{2+} for Sr^{2+} mainly causes bending of the B−X−B angles rather than the decreasing of the B−X bond lengths. This is corroborated by an additional band structure calculation for Ca_2FeMoO_6 using the tetragonal structure of Sr_2FeMoO_6, which gives results almost identical to those in Figure 11a.

From the above considerations, an increase in Ca content (i.e., chemical pressure) in $(Sr_{2-x}Ca_x)FeMoO_6$ decreases cos ω and thus decreases the bandwidth, which should also lead to a fall in the conductivity. This is inconsistent with the observed increase in conductivity with x and implies that the dominant factor is the overlap of Fe 3d:t_{2g} and Mo 4d:t_{2g} orbitals. Conductivity in this system can be viewed as arising from electron transfer from Fe^{2+} to Mo^{6+} so the influence of Ca content x on the charge-transfer y in $(Sr_{2-x}Ca_x)Fe^{2+y}Mo^{6-y}O_6$ is very important. A simple predictor for the change in y is to compare the sums of ionic radii for the extremes of y. For $y = 0$, $r(Fe^{2+}) = 0.78$ Å and $r(Mo^{6+}) = 0.59$ Å and their sum is 1.37 Å; at $y = 1$, $r(Fe^{3+}) = 0.645$ Å and $r(Mo^{5+}) = 0.61$ Å, giving a sum of 1.255 Å. Hence, an increase in Ca content will tend to shift the charge balance toward Fe^{3+} + Mo^{5+} as this allows the transition metal oxide framework to contract, and so y increases with x. This increase in band overlap is supported by our conductivity, XANES, and band calculation results.

(31) Medarde, M.; Mesot, J.; Lacorre, P.; Rosenkranz, S.; Fischer, P.; Gobrecht, K. *Phys. Rev. B* **1995**, *52*, 9248.

Recently, Viola et al.[32] speculate that a mixed Mo^{6+}–Mo^{5+} valence in reduced Sr_2CoMoO_{6-d} samples (where Co has a valence of 2+) leads to a dramatic enhancement of the electronic conductivity, as compared to that of the pure Mo^{6+} sample. This finding is similar to our results, which is due to a decrease in Mo valence, giving a better band overlap.

Conclusions

The increasing Ca content in $(Sr_{2-x}Ca_x)FeMoO_6$ samples increases the magnetic moment close to the theoretical value due to a reduction of Fe/Mo anti-site disorder. An increase of conductivity with Ca doping is also observed, resulting from an increase in the Fe 3d–Mo 4d band overlap. This is explained from simple ionic size arguments and is supported by XANES spectra and band structure calculations. We conclude that the chemical pressure effects of doping Ca from the Sr site is an important factor in control of the charge transfer and hence the electrical and magnetic properties of the magnetoresistive Sr_2FeMoO_6-type materials.

Acknowledgment. The National Science Council of the Republic of China under Grants NSC 90-2113-M-002-048 and NSC 90-2112-M-002-040 supported this work.

CM020773H

(32) Viola, M. C.; Martínze-Lope, M. J.; Alonso, J. A.; Velasco, P.; Martínze, J. L.; Pedregosa, J. C.; Carbonio, R. E.; Fernández-Díaz, M. T. *Chem. Mater.* **2002**, *14*, 812.